Strong dineutron correlation in ^{8}He and ^{18}C

K. Hagino,[1] N. Takahashi,[1] and H. Sagawa[2]
[1]*Department of Physics, Tohoku University, Sendai, 980-8578, Japan*
[2]*Center for Mathematical Sciences, University of Aizu, Aizu-Wakamatsu, Fukushima 965-8560, Japan*
(Received 20 March 2008; published 28 May 2008)

We study the spatial structure of four valence neutrons in the ground state of ^{8}He and ^{18}C nuclei using a core+4n model. For this purpose, we employ a density-dependent contact interaction among the valence neutrons, and solve the five-body Hamiltonian in the Hartree-Fock-Bogoliubov (HFB) approximation. We show that two neutrons with the coupled spin of $S = 0$ exhibit a strong dineutron correlation around the surface of these nuclei, whereas the correlation between the two dineutrons is much weaker. Our calculation indicates that the probability of the $(1p_{3/2})^4$ and $[(1p_{3/2})^2(p_{1/2})^2]$ configurations in the ground state wave function of ^{8}He nucleus is 34.9% and 23.7%, respectively. This is consistent with the recent experimental finding with the ^{8}He$(p, t)^{6}$He reaction, that is, the ground state wave function of ^{8}He deviates significantly from the pure $(1p_{3/2})^4$ structure.

DOI: 10.1103/PhysRevC.77.054317 PACS number(s): 21.10.Gv, 21.30.Fe, 21.45.−v, 27.20.+n

I. INTRODUCTION

It has been well recognized that the pairing correlation and couplings to the continuum spectra play an essential role in weakly bound nuclei [1,2]. Although the dineutron structure as a consequence of the pairing correlation has been suggested for some time in ^{11}Li and ^{6}He nuclei [1,3], it was only recently that a strong indication of its existence was obtained experimentally in the Coulomb dissociation of ^{11}Li [4]. The new measurement has stimulated lots of theoretical discussions on the dineutron correlation, not only in the 2n halo nuclei, ^{11}Li and ^{6}He [5–8], but also in medium-heavy neutron-rich nuclei [9,10] as well as in infinite neutron matter [11,12].

In Ref. [7], we have studied the behavior of valence neutrons in ^{11}Li at various positions from the center to the surface of the nucleus. We have found that (i) the two-neutron wave function oscillates near the center whereas it becomes similar to that for a bound state around the nuclear surface, and (ii) the local pair coherence length has a well pronounced minimum around the nuclear surface. This result clearly indicates that a strong dineutron correlation between the valence neutrons is present on the surface of the nucleus.

An important next question is how the spatial structure of valence neutrons evolves from that in the 2n-halo nucleus, ^{11}Li, when there are more numbers of neutrons. Although Refs. [9,10] have partially addressed this question by studying a two-particle density for medium-heavy neutron-rich nuclei, one would also need to explore a four-particle density, or many-particle density in general, in order to shed light on the ground state properties of neutron-skin nuclei.

For this purpose, ^{8}He makes the most suitable nucleus to study. ^{8}He is expected to have the $\alpha + 4n$ structure [13–20], and thus provides a bridge between the 2n-halo nuclei and heavier skin nuclei. We mention that the spatial structure of the four valence neutrons in ^{8}He has been discussed in Ref. [16], where the authors constructed the ground state wave function by assuming that the four neutrons occupy the $1p_{3/2}$ state in a harmonic oscillator potential. However, this model is too simplistic, since it completely neglects the pairing correlation and the continuum couplings. Notice that the mixing of many partial wave components, especially those with different parities, is essential in order to have a spatially compact dineutron structure [9,10,21]. In fact, we do not see any indication of dineutron correlation in the result of Ref. [16] (see Fig. 2 of Ref. [16]), despite that the dineutron structure is expected to be enhanced in many neutron-rich nuclei [7,9,10].

The purpose of this paper is to reinvestigate the spatial structure of the four valence neutrons in ^{8}He by taking into account consistently the pairing and the continuum effects. To this end, we use the core+4n model, and diagonalize the five-body Hamiltonian in the Hartree-Fock-Bogoliubov (HFB) approximation. We also study the ^{18}C nucleus as another nucleus which is expected to have the core+4n structure [22–25]. We will demonstrate below that the pairing correlation leads to the strong dineutron structure in ^{8}He and ^{18}C, in contrast to the result of Ref. [16].

The paper is organized as follows. In Sec. II, we detail the HFB method based on the core+4n model. In Sec. III, we apply the method to ^{6}He, where the result of the exact diagonalization of the three-body $(\alpha + n + n)$ Hamiltonian has been obtained [6,26]. We compare the HFB result with the exact result, and discuss the applicability of the HFB method for the study of the spatial structure of valence neutrons. In Sec. IV, we present the results for the ^{8}He and ^{18}C nuclei. We discuss the two- and four-particle densities, as well as the probability of the single-particle components in the ground state wave function. We then summarize the paper in Sec. V.

II. HFB METHOD FOR A CORE+4nMODEL

A. HFB equations

In order to study the structure of the ^{8}He and ^{18}C nuclei, we employ the core+4n model, and consider the following Hamiltonian:

$$H = \sum_{i=1}^{4}\left[\frac{\boldsymbol{p}_i^2}{2m_N} + V_{nC}(r_i)\right] + \sum_{i<j} v_{nn}(\boldsymbol{r}_i - \boldsymbol{r}_j) - T_{\text{c.m.}}, \tag{1}$$

$$\sim \sum_{i=1}^{4}\left[\frac{\boldsymbol{p}_i^2}{2m_N}\left(1-\frac{1}{A}\right)+V_{nC}(r_i)\right]+\sum_{i<j}v_{nn}(\boldsymbol{r}_i-\boldsymbol{r}_j), \tag{2}$$

$$\equiv \sum_{i=1}^{4}\left[\frac{\boldsymbol{p}_i^2}{2m}+V_{nC}(r_i)\right]+\sum_{i<j}v_{nn}(\boldsymbol{r}_i-\boldsymbol{r}_j). \tag{3}$$

Here, m_N is the nucleon mass, A is the mass number of the nucleus, V_{nC} is a potential between a valence neutron and the core nucleus, and v_{nn} is the pairing interaction among the valence neutrons. $T_{\rm c.m.}$ is the kinetic energy for the center of mass motion of the whole nucleus. In Refs. [6,26], the center of mass motion is treated exactly by introducing the recoil kinetic energy of the core nucleus (see Ref. [14] for the derivation of the recoil term). In this paper, we approximate the treatment by taking only the diagonal components in $T_{\rm c.m.}$, as is often done in mean-field calculations [27] (notice that the off-diagonal components contribute only to the exchange part of the mean-field potential). This leads to the renormalization of the nucleon mass, $m = A/(A-1)\cdot m_N$.

Although the five-body Hamiltonian (3) could be diagonalized exactly, e.g., with the stochastic variational method [15], we seek an approximate solution using the HFB method [2,28–30]. The ground state wave function in the HFB method is given by [28]

$$|\mathrm{HFB}\rangle = \prod_k \hat{\beta}_k|0\rangle, \tag{4}$$

where the quasiparticle operator $\hat{\beta}_k$ is given by

$$\hat{\beta}_k = \int d\boldsymbol{r}\sum_\sigma (U_k^*(\boldsymbol{r},\sigma)a_{\boldsymbol{r}\sigma}+V_k^*(\boldsymbol{r},\sigma)a_{\boldsymbol{r}\sigma}^\dagger). \tag{5}$$

In this equation, $\sigma = \pm 1/2$ is the spin coordinate, $a_{\boldsymbol{r}\sigma}^\dagger$ is the creation operator of nucleons at the position $\boldsymbol{r}$ and σ, and U_k and V_k are the HFB quasi-particle wave functions. In this paper, we employ a density-dependent pairing interaction [1] for v_{nn} given by

$$v_{nn}(\boldsymbol{r},\boldsymbol{r}') = V_0\left(1-\frac{\rho_t(\bar{\boldsymbol{r}})}{\rho_0}\right)\delta(\boldsymbol{r}-\boldsymbol{r}'), \tag{6}$$

where $\bar{\boldsymbol{r}} = (\boldsymbol{r}+\boldsymbol{r}')/2$ and $\rho_t(\boldsymbol{r}) = \rho_C(\boldsymbol{r})+\rho_v(\boldsymbol{r})$ is the total density, ρ_C and ρ_v being the density of the core nucleus and the valence neutrons, respectively. For this interaction, the expectation value of the Hamiltonian (3) with the HFB state (4) reads [2]

$$E = \langle\mathrm{HFB}|H|\mathrm{HFB}\rangle, \tag{7}$$

$$= \int d\boldsymbol{r}\left(\frac{\hbar^2}{2m}\tau(\boldsymbol{r})+V_{nC}(\boldsymbol{r})\rho_v(\boldsymbol{r})\right) + \frac{V_0}{4}\int d\boldsymbol{r}\left(1-\frac{\rho_t(\boldsymbol{r})}{\rho_0}\right)(\rho_v(\boldsymbol{r})^2+\tilde{\rho}_v(\boldsymbol{r})^2), \tag{8}$$

where the kinetic energy density $\tau(\boldsymbol{r})$, the particle density $\rho_v(\boldsymbol{r})$, and the pairing density $\tilde{\rho}_v(\boldsymbol{r})$ are given by

$$\tau(\boldsymbol{r}) = \sum_k\sum_\sigma |\nabla V_k(\boldsymbol{r},\sigma)|^2, \tag{9}$$

$$\rho_v(\boldsymbol{r}) = \sum_k\sum_\sigma |V_k(\boldsymbol{r},\sigma)|^2, \tag{10}$$

$$\tilde{\rho}_v(\boldsymbol{r}) = -\sum_k\sum_\sigma V_k(\boldsymbol{r},\sigma)U_k^*(\boldsymbol{r},\sigma), \tag{11}$$

respectively. In deriving Eq. (8), we have used the properties of time-reversal symmetry [2].

The equations for the HFB wave functions V_k and U_k are obtained by taking the variation of the energy expectation value (8) with respect to the particle and the pairing densities. This leads to the HFB equations in the coordinate space representation [2,29,30],

$$\begin{pmatrix}\hat{h}-\lambda & \Delta(r)\\ \Delta(r) & -\hat{h}+\lambda\end{pmatrix}\begin{pmatrix}U_k(\boldsymbol{r},\sigma)\\ V_k(\boldsymbol{r},\sigma)\end{pmatrix} = E_k\begin{pmatrix}U_k(\boldsymbol{r},\sigma)\\ V_k(\boldsymbol{r},\sigma)\end{pmatrix}, \tag{12}$$

where λ is the Fermi energy. The mean-field Hamiltonian $\hat{h}$ is given by

$$\hat{h} = \frac{\delta E}{\delta\rho_v}, \tag{13}$$

$$= -\frac{\hbar^2}{2m}\nabla^2+V_{nC}(\boldsymbol{r})+\frac{V_0}{2}\left(1-\frac{\rho_t(\boldsymbol{r})}{\rho_0}\right)\rho_v(\boldsymbol{r}) - \frac{1}{4}V_0\frac{\rho_v(\boldsymbol{r})^2+\tilde{\rho}_v(\boldsymbol{r})^2}{\rho_0}, \tag{14}$$

while the pairing potential $\Delta(r)$ is given by

$$\Delta(r) = \frac{\delta E}{\delta\tilde{\rho}_v}, \tag{15}$$

$$= \frac{V_0}{2}\left(1-\frac{\rho_t(\boldsymbol{r})}{\rho_0}\right)\tilde{\rho}_v(\boldsymbol{r}). \tag{16}$$

We solve the HFB equations (12) self-consistently by expanding the HFB wave functions on the eigenfunctions of the mean-field Hamiltonian $\hat{h}$ [31]. In doing so, we respect the Pauli principle and explicitly exclude those states which are occupied by the neutrons in the core nucleus. Notice that the HFB method could be applied to light neutron-rich nuclei without introducing the core nucleus [32,33]. We nevertheless treat only the valence neutrons explicitly, since it is not straightforward to separate between the core and the valence parts from the HFB ground state wave function (4).

B. Two- and four-particle densities

In order to discuss the spatial structure of the valence neutrons, we compute the two- and four-particle densities using the solution of the HFB equations. Using Wick's theorem, the two-particle density can be expressed as [9]

$$\rho_2(\boldsymbol{r}\sigma,\boldsymbol{r}'\sigma') = \langle\mathrm{HFB}|a_{\boldsymbol{r}\sigma}^\dagger a_{\boldsymbol{r}'\sigma'}^\dagger a_{\boldsymbol{r}'\sigma'}a_{\boldsymbol{r}\sigma}|\mathrm{HFB}\rangle, \tag{17}$$

$$= |\tilde{\rho}_v(\boldsymbol{r}\sigma,\boldsymbol{r}'\tilde{\sigma}')|^2-|\rho_v(\boldsymbol{r}\sigma,\boldsymbol{r}'\sigma')|^2 + \rho_v(\boldsymbol{r}\sigma)\rho_v(\boldsymbol{r}'\sigma'), \tag{18}$$

where $\tilde{\sigma} = -\sigma$, and the off-diagonal components of the densities are given as [see Eqs. (10) and (11)],

$$\rho_v(\boldsymbol{r}\sigma,\boldsymbol{r}'\sigma') = \sum_k V_k(\boldsymbol{r},\sigma)V_k^*(\boldsymbol{r}',\sigma'), \tag{19}$$

$$\tilde{\rho}_v(\boldsymbol{r}\sigma, \boldsymbol{r}'\sigma') = -\sum_k V_k(\boldsymbol{r}, \sigma) U_k^*(\boldsymbol{r}', \sigma'). \tag{20}$$

In order to evaluate the four-particle density,

$$\rho_4(x_1, x_2, x_3, x_4) = \langle \mathrm{HFB} | a_{x_1}^\dagger a_{x_2}^\dagger a_{x_3}^\dagger a_{x_4}^\dagger a_{x_4} a_{x_3} a_{x_2} a_{x_1} | \mathrm{HFB} \rangle, \tag{21}$$

where $x = (\boldsymbol{r}, \sigma)$, we find it useful to express the HFB ground state wave function, Eq. (4), using the canonical basis. The canonical basis function ψ is the eigenfunction of the density matrix (19) and satisfies [2,28]

$$\sum_{\sigma'} \int d\boldsymbol{r}' \rho_v(\boldsymbol{r}\sigma, \boldsymbol{r}'\sigma') \psi_p(\boldsymbol{r}', \sigma') = v_p^2 \psi_p(\boldsymbol{r}, \sigma). \tag{22}$$

In this paper, we construct the canonical basis by expanding ψ_p on the HF basis, as is done for the HFB wave functions (see the previous subsection). Using the canonical basis, the HFB ground state wave function is given in the BCS form as [2,28]

$$|\mathrm{HFB}\rangle = \prod_{p>0} \left(u_p + v_p a_p^\dagger a_{\bar{p}}^\dagger\right)|0\rangle, \tag{23}$$

$$\propto \exp\left(\sum_{p>0} \frac{v_p}{u_p} a_p^\dagger a_{\bar{p}}^\dagger\right)|0\rangle, \tag{24}$$

where $u_p = \sqrt{1 - v_p^2}$ and $\bar{p}$ is the time-reversed state of p. Since the creation operator for the canonical basis, $a_p^\dagger$, is related to the creation operator in the coordinate space, $a_{\boldsymbol{r}\sigma}^\dagger$, as

$$a_p^\dagger = \int d\boldsymbol{r} \sum_\sigma \psi_p(\boldsymbol{r}, \sigma) a_{\boldsymbol{r}\sigma}^\dagger, \tag{25}$$

Eq. (24) is transformed to [2]

$$|\mathrm{HFB}\rangle \propto \exp\left(-\frac{1}{2}\int d\boldsymbol{r} d\boldsymbol{r}' \sum_{\sigma,\sigma'} Z(\boldsymbol{r}\sigma, \boldsymbol{r}'\sigma') a_{\boldsymbol{r}\sigma}^\dagger a_{\boldsymbol{r}'\sigma'}^\dagger\right)|0\rangle, \tag{26}$$

with

$$Z(\boldsymbol{r}\sigma, \boldsymbol{r}'\sigma') = -2\sum_{p>0} \frac{v_p}{u_p} \psi_p(\boldsymbol{r}, \sigma)\psi_{\bar{p}}(\boldsymbol{r}', \sigma'). \tag{27}$$

To evaluate the four-particle density, Eq. (21), we first perform the particle number projection onto the HFB state,

$$\hat{P}_N|\mathrm{HFB}\rangle \propto \left(-\frac{1}{2}\int d\boldsymbol{r} d\boldsymbol{r}' \sum_{\sigma,\sigma'} Z(\boldsymbol{r}\sigma, \boldsymbol{r}'\sigma') a_{\boldsymbol{r}\sigma}^\dagger a_{\boldsymbol{r}'\sigma'}^\dagger\right)^2 |0\rangle. \tag{28}$$

The four-particle density is then obtained as

$$\rho_4(x_1, x_2, x_3, x_4) \propto |f(x_1, x_2, x_3, x_4)|^2, \tag{29}$$

with

$$\begin{aligned} &f(x_1, x_2, x_3, x_4) \\ &= (Z(x_1, x_2) - Z(x_2, x_1))(Z(x_3, x_4) - Z(x_4, x_3)) \\ &+ (Z(x_1, x_3) - Z(x_3, x_1))(Z(x_4, x_2) - Z(x_2, x_4)) \\ &+ (Z(x_1, x_4) - Z(x_4, x_1))(Z(x_2, x_3) - Z(x_3, x_2)). \end{aligned} \tag{30}$$

C. Probability for shell model configurations

Using the canonical basis representation of the HFB state, Eq. (23), one can also calculate the probability for a shell model configuration, $[(k\bar{k})(k'\bar{k}')]$, for the four-particle systems when k and k' represent the canonical basis states. It is given by

$$P_{k^2k'^2} = \frac{1}{\mathcal{N}}|\langle (k\bar{k})(k'\bar{k}')|\mathrm{HFB}\rangle|^2 = \frac{1}{\mathcal{N}} v_k^2 v_{k'}^2 \prod_{p\neq k,k'(>0)} u_p^2, \tag{31}$$

where the normalization factor $\mathcal{N}$ reads

$$\begin{aligned} \mathcal{N} &= \langle \mathrm{HFB}|\hat{P}_{N=4}|\mathrm{HFB}\rangle \\ &= \frac{1}{2\pi}\int_0^{2\pi} d\phi e^{-4i\phi} \prod_{p>0} \left(u_p^2 + e^{2i\phi} v_p^2\right). \end{aligned} \tag{32}$$

Here, we have used the explicit form of the number projection operator [28],

$$\hat{P}_N = \frac{1}{2\pi}\int_0^{2\pi} d\phi e^{i\phi(\hat{N}-N)}. \tag{33}$$

If the angular momentum components are explicitly expressed, the probability (31) reads

$$P_{(lj)^4} = \frac{1}{\mathcal{N}} \cdot \binom{\Omega_j}{2} \left(v_{lj}^2\right)^2 \left(u_{lj}^2\right)^{\Omega_j - 2} \prod_{l'j'\neq lj} \left(u_{l'j'}^2\right)^{\Omega_{j'}}, \tag{34}$$

for the $(lj)^4$ configuration, while

$$\begin{aligned} P_{(lj)^2(l'j')^2} = \frac{1}{\mathcal{N}} \cdot \Omega_j \Omega_{j'} v_{lj}^2 \left(u_{lj}^2\right)^{\Omega_j - 1} v_{l'j'}^2 \left(u_{l'j'}^2\right)^{\Omega_{j'}-1} \\ \times \prod_{l''j''\neq lj, l'j'} \left(u_{l''j''}^2\right)^{\Omega_{j''}}, \end{aligned} \tag{35}$$

for the $(lj)^2(l'j')^2$ configuration with $lj \neq l'j'$. In these equations, $\Omega_j = (2j+1)/2$ is the pair degeneracy for the angular momentum j state.

III. APPLICABILITY OF HFB METHOD: TEST ON ^{6}He NUCLEUS

Let us now numerically solve the HFB equations and discuss the spatial structure of neutron-rich nuclei. Before we do this, however, we first examine the applicability of the HFB method by applying it to the three-body model of ^{6}He nucleus [6,26]. This model has been solved exactly by diagonalizing the Hamiltonian matrix. A comparison of the HFB solution with the exact result for this model will provide an idea on whether the HFB method is good enough to discuss the dineutron correlation in neutron-rich nuclei.

To this end, we use the same neutron-core potential, V_{nC}, and the same pairing interaction v_{nn} as in Refs. [6,26]. The neutron-core potential is taken as a Woods-Saxon form, together with a spin-orbit interaction. Since we use the renormalized mass m [see Eq. (3)] instead of the reduced mass, we multiply the factor $(A-1)/A \cdot A_C/(A_C+1)$, where A_C is the mass number of the core nucleus, following the prescription

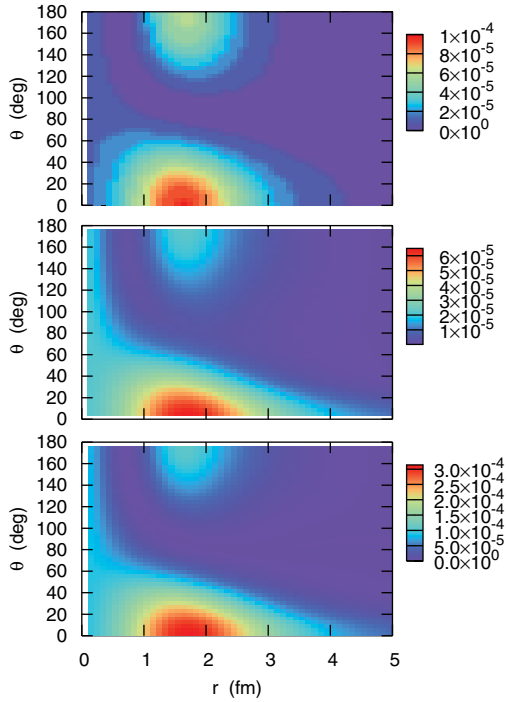

FIG. 1. (Color online) The $S = 0$ component of the two-particle density for ^{6}He as a function of $r_1 = r_2 = r$ and the angle between the valence neutrons, θ. The top panel shows the exact solution of the three-body model, while the middle panel is obtained with the HFB method. The bottom panel shows the result of the HFB+particle number projection.

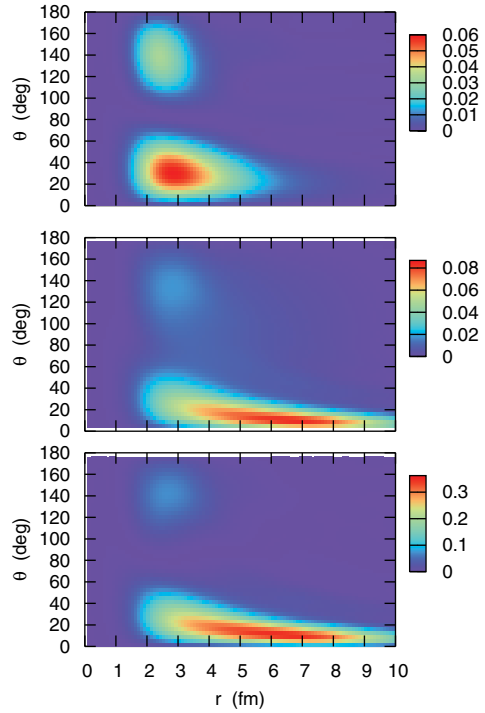

FIG. 2. (Color online) Same as Fig. 1, but with a multiplicative factor of $8\pi^2 r^4 \sin\theta$.

given in Ref. [26]. The pairing interaction is given as

$$v_{nn}(\boldsymbol{r}, \boldsymbol{r}') = \delta(\boldsymbol{r} - \boldsymbol{r}') \left(v_0 + \frac{v_\rho}{1 + \exp[(r - R_\rho)/a_\rho]} \right). \quad (36)$$

We multiply an overall scaling factor to this interaction so that the two-neutron separation energy of ^{6}He is reproduced with the HFB method. We use the same value for all the other parameters as in Ref. [6]. Note that the last term in Eq. (14) disappears for the pairing interaction given by Eq. (36), since the interaction does not depend explicitly on the density, but the density dependence is parametrized by the Fermi function.

Figure 1 shows the two-particle density for ^{6}He in the $S = 0$ channel, that is, $\rho_2(\boldsymbol{r}_1 \uparrow, \boldsymbol{r}_2 \downarrow)$. As we have done in Ref. [6], we set $r_1 = r_2 \equiv r$ and plot the density as a function of r and the relative angle between the spin up and down neutrons, θ. Figure 2 shows the same two-particle density, but we multiply the factor $8\pi^2 r^4 \sin\theta$ [6]. The top panels in these figures show the exact solution of the three-body Hamiltonian [6], while the middle panels are for the HFB results. One can clearly see that the localization of the two-particle density around $\theta \sim 0$ in the three-body model is well reproduced by the HFB method, although the HFB density has a somewhat longer tail and the density around $\theta \sim \pi$ is largely suppressed. The localization of the two-particle density is nothing but the manifestation of the strong dineutron correlation in a halo nucleus ^{6}He. The longer tail of the HFB density may be due to the asymptotic behavior of the pair density $\tilde{\rho}_v(\boldsymbol{r}_1 \uparrow, \boldsymbol{r}_2 \downarrow)$ in Eq. (18), which is different from that of the normal density $\rho_v(\boldsymbol{r}_1 \uparrow, \boldsymbol{r}_2 \downarrow)$ [2].

The similarity between the exact and the HFB results for the two-particle density is rather striking, and it is clear that the HFB method can be utilized to discuss, at least qualitatively, the strong dineutron correlation in neutron-rich nuclei.

We also study the effect of particle number projection on the two-particle density. The bottom panels in Figs. 1 and 2 are obtained by taking the number projection onto the HFB ground state (with the variation before projection (VBP) scheme [34]) in a similar way as in Eq. (28). The two-particle density thus obtained is not normalized and the scale is different between the middle and the bottom panels. However, we can see that the dependence of the two-particle density on r and θ is almost the same between the two panels. Therefore, we conclude that the effect of number projection is rather small as far as the two-particle density is concerned, although the projection might still affect the density if the variation after projection (VAP) scheme is employed.

Table I summarizes the occupation probabilities for the ^{6}He nucleus. Although the absolute value is somewhat smaller,

TABLE I. Comparison of the exact and the HFB results for the occupation probabilities in the ground state of ^{6}He.

Configuration	Exact [6]	HFB
$(s_{1/2})^2$	3.04%	7.25%
$(p_{1/2})^2$	4.85%	9.21%
$(p_{3/2})^2$	83.0%	57.4%
$(d_{3/2})^2$	1.47%	3.86%
$(d_{5/2})^2$	6.11%	6.85%
$(f_{5/2})^2$	0.035%	2.30%
$(f_{7/2})^2$	0.075%	3.33%

TABLE II. The results of the HFB calculation for the Fermi energy λ and the root-mean-square (rms) radius, $r_{\rm rms}$, for the ^{8}He and ^{18}C nuclei.

Nucleus	$E_{\rm g.s.}$ (MeV)	λ (MeV)	$r_{\rm rms}$ (fm)	$r_{\rm rms}^{\rm (exp)}$ (fm)
^{8}He	−3.112	−0.0715	3.23	2.49 ± 0.04 [13]
^{18}C	−10.514	−2.522	2.92	2.90 ± 0.19 [38]

the HFB well reproduces the dominance of the $(p_{3/2})^2$ configuration in the ground state wave function. Again, the HFB method provides a good estimate of the ground state properties of neutron-rich nuclei even when the number of particle is as small as two.

IV. DINEUTRON CORRELATION IN ^{8}He AND ^{18}C

We now solve the HFB equations for the ^{8}He and ^{18}C nuclei. We use the same neutron-core potential, V_{nC}, for ^{8}He as in Refs. [6,26], while we use set D in Refs. [24,25] for the ^{18}C nucleus. As in the previous section, these potentials are scaled by a factor of $(A-1)/A \cdot A_C/(A_C+1)$. For the core density, ρ_C, we use those in Refs. [16,35]. We determine the strength of the pairing interaction so that the experimental ground state energy relative to the core+4n threshold, $E = -3.112$ MeV for ^{8}He and -10.385 MeV for ^{18}C, is reproduced with $\rho_0 = 0.32$ fm^{-3} (i.e., the mixed pairing interaction [36,37]). With the cut-off energy of $\epsilon_{\rm cut} + \lambda = 40$ MeV in the single-particle space, this leads to $V_0 = -502$ MeV fm^3 for ^{8}He and $V_0 = -538$ MeV fm^3 for ^{18}C.

The results of the HFB calculation are summarized in Table II. Although our purpose in this paper is not to reproduce the experimental data, but to discuss qualitatively the dineutron correlation in ^{8}He and ^{18}C, we notice that the root-mean-square radius for the ^{18}C nucleus is well reproduced with the present calculation. The mean-field potential in Eq. (14) is shown in Fig. 3, in which the dashed and the solid lines correspond to the neutron-core potential, V_{nC}, and the total mean-field potential, respectively. The difference between the two potentials originates from the effect of pairing correlations among the valence particles on the mean field potential. As a consequence, the mean-field potential for ^{8}He posses one bound single-particle state while the neutron-^{4}He potential V_{nC} alone does not hold any bound single-particle state, reflecting the Borromean nature of the ^{6}He nucleus [6,26]. For the ^{18}C nucleus, the same effect shifts the single-particle energy from -1.072 to -1.768 MeV for the $2s_{1/2}$ state and from -0.414 to -1.664 MeV for $1d_{5/2}$.

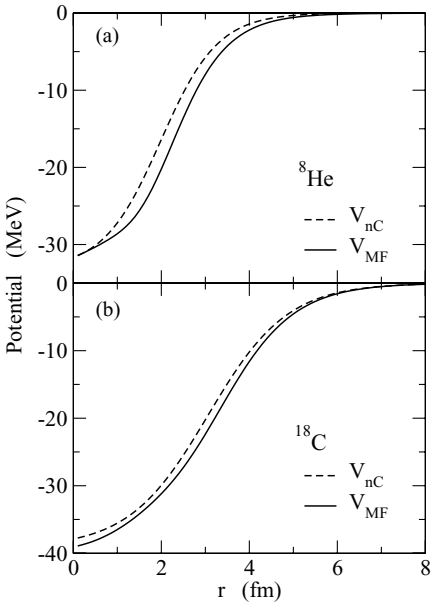

FIG. 3. The mean-field potential for ^{8}He (the upper panel) and for ^{18}C (the lower panel). The dashed line shows the neutron-core potential, V_{nC}, while the solid line is for the total mean-field potential in the solution of the HFB equations.

TABLE III. Probability of a few shell model configurations in the HFB ground state wave function for ^{8}He and ^{18}C.

Nucleus	Configuration	Probability (%)
^{8}He	$[(1p_{3/2})^4]$	34.9
	$[(1p_{3/2})^2(p_{1/2})^2]$	23.7
	$[(p_{3/2})^2(d_{5/2})^2]$	10.7
	$[(s_{1/2})^2(p_{3/2})^2]$	7.8
^{18}C	$[(1d_{5/2})^4]$	32.2
	$[(1d_{5/2})^2(2s_{1/2})^2]$	26.2
	$[(1d_{5/2})^2(d_{3/2})^2]$	11.8
	$[(d_{5/2})^2(f_{7/2})^2]$	7.17

The probability for a few single-particle components in the ground state wave function is listed in Table III. Notice that these shell model configurations are those represented by the canonical basis, which has a large spatial extension for a weakly bound orbital. For the ^{8}He nucleus, although the largest probability is found in the $[(1p_{3/2})^4]$ configuration, the other components also have an appreciable probability. Therefore, this nucleus largely deviates from the pure $[(1p_{3/2})^4]$ configuration, in accordance with the recent experimental finding with the ^{8}He$(p,t)^6$He reaction [39]. For the ^{18}C nucleus, the ground state wave function mainly consists of the $[(1d_{5/2})^4]$ and the $[(1d_{5/2})^2(2s_{1/2})^2]$ configurations, while the $[(1d_{5/2})^2(d_{3/2})^2]$ and the $[(d_{5/2})^2(f_{7/2})^2]$ configurations are also appreciable in Table III.

The top panel in Figs. 4 and 5 shows the two-particle density, $\rho_2(r, \hat{\boldsymbol{r}} = 0, \uparrow; r, \hat{\boldsymbol{r}}, \downarrow)$, for ^{8}He and ^{18}C, respectively. The middle panels in these figures show the same two-particle density, but with the multiplicative factor of $8\pi^2 r^4 \sin\theta$. For both the ^{8}He and ^{18}C nuclei, one clearly finds a strong concentration of two-particle density around $\theta \sim 0$ at around the nuclear surface. This is similar to what has been found in the Borromean nuclei, ^{11}Li and ^{6}He [6,26] (see also Figs. 1 and 2), and indicates clearly the strong dineutron correlation [7,9,10] in these nuclei.

Since the strong dineutron structure is apparent for spin-up and spin-down neutrons in these nuclei, we next plot the four-particle density for the two-dineutron configuration,

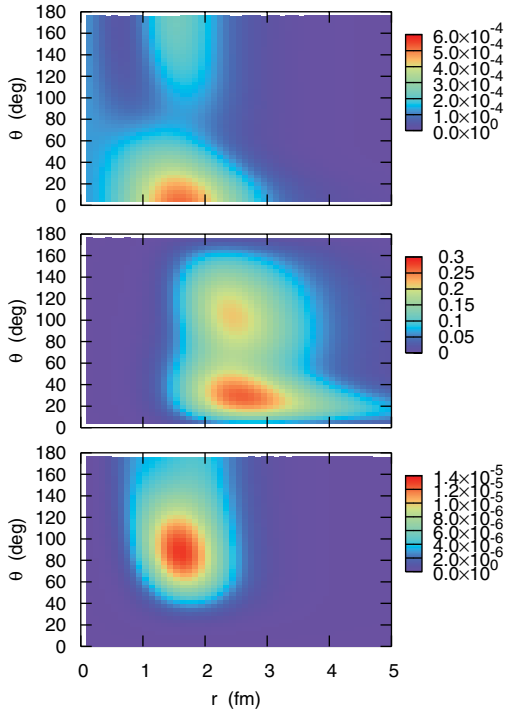

FIG. 4. (Color online) The two-particle density, $\rho_2(r, \hat{\boldsymbol{r}} = 0, \uparrow; r, \hat{\boldsymbol{r}}, \downarrow)$, for the ^{8}He nucleus as a function of $r_1 = r_2 = r$ and the relative angle θ between a spin-up and a spin-down neutrons (the top panel). The middle panel shows the same two-particle density multiplied by a factor $8\pi^2 r^4 \sin\theta$, while the bottom panel is for the four-particle density for the dineutron-dineutron configuration.

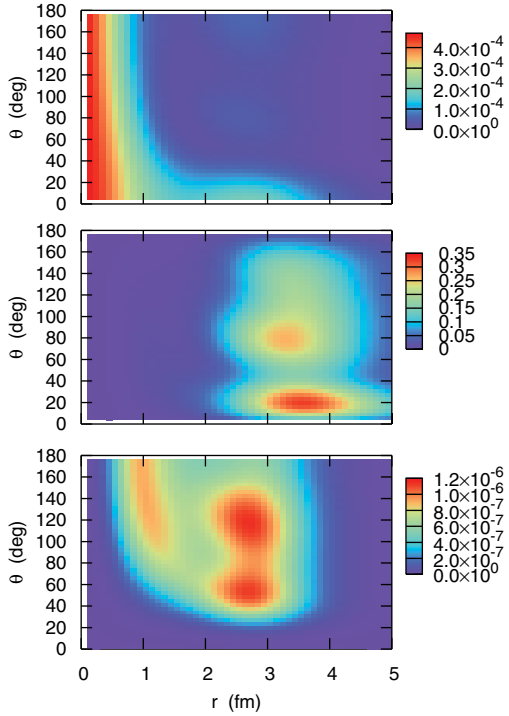

FIG. 5. (Color online) Same as Fig. 4, but for ^{18}C.

that is, the four-particle density with $x_1 = (r, \hat{\boldsymbol{r}} = 0, \uparrow)$, $x_2 = (r, \hat{\boldsymbol{r}} = 0, \downarrow)$, $x_3 = (r, \hat{\boldsymbol{r}}, \uparrow)$, and $x_4 = (r, \hat{\boldsymbol{r}}, \downarrow)$ in Eq. (21). This is plotted in the bottom panels in Figs. 4 and 5 for ^{8}He and ^{18}C, respectively. For the ^{8}He nucleus, the four-particle density for the dineutron-dineutron configuration has a peak around $\theta \sim \pi/2$. A similar result has been obtained with a three-body model calculation with the dineutron clusters, that is, $\alpha + n^2 + n^2$ [17]. The peak around $\theta \sim \pi/2$ arises from the main component of the wave function, that is, the $[(1p_{3/2})^4]$ configuration, for which the four-particle density is proportional to $\sin^4\theta \propto |Y_{11}|^4$. For the ^{18}C nucleus, the four-particle density has two peaks, one around $\theta \sim 54^\circ$ and the other around $\theta \sim 118^\circ$. This can again be understood in terms of the $[(1d_{5/2})^4]$ configuration, for which the four-particle density is proportional to $(3|Y_{22}|^2 + 2|Y_{21}|^2)^2$.

To demonstrate more clearly the similarity between the four-particle density to that for the main components, the bottom panels of Figs. 6 and 7 show the four-particle density for the $[(1p_{3/2})^4]$ and $[(1d_{5/2})^4]$ configurations in the neutron-core potential V_{nC}, respectively. To this end, we adjust the depth of the neutron-core potential so that the energy of the $1p_{3/2}$ and $1d_{5/2}$ states is a quarter the energy of ^{8}He and ^{18}C, respectively. The similarity between the four-particle density for the correlated wave functions (Figs. 4 and 5) and that for the uncorrelated wave functions (Figs. 6 and 7) is apparent. This is a natural consequence of a short range nature of nuclear interaction: the two neutrons with the same spin have to be far apart in space due to the Pauli principle and thus their distance is likely larger than the range of the nuclear interaction. As a consequence, the interaction between the two dineutrons becomes weak, despite that the two neutrons in the *same* dineutron having different spins strongly interact with each other. From this consideration, we conclude that the two

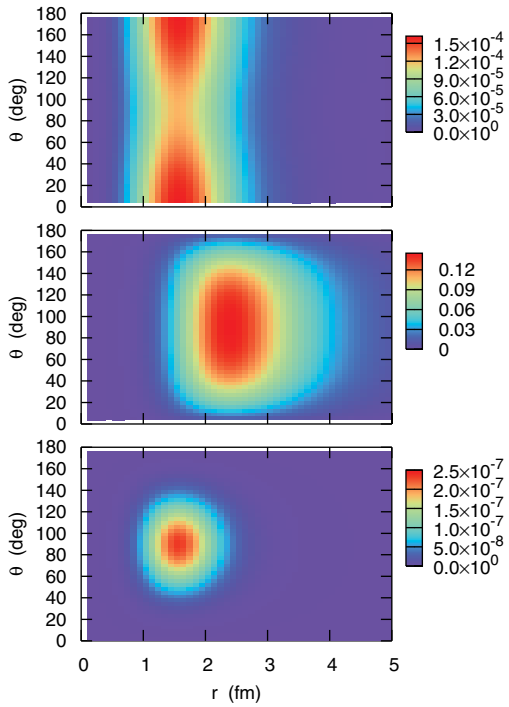

FIG. 6. (Color online) Same as Fig.4, but for the uncorrelated $[(1p_{3/2})^4]$ configuration for the ^{8}He nucleus.

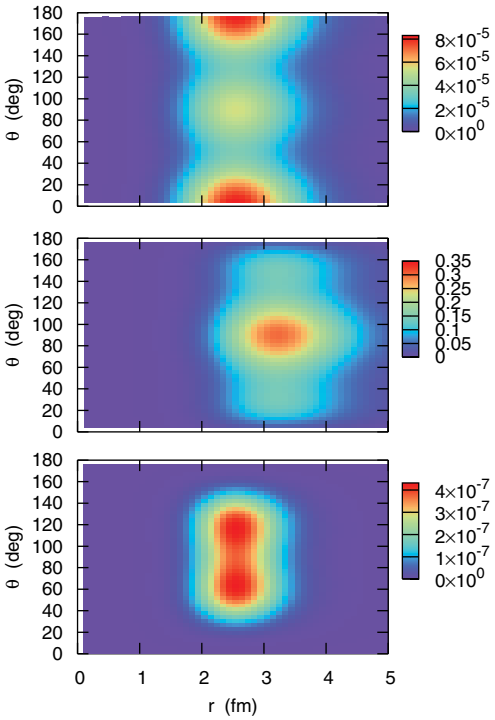

FIG. 7. (Color online) Same as Fig. 5, but for the uncorrelated $[(1d_{5/2})^4]$ configuration for the ^{18}C nucleus.

dineutrons are moving rather freely in the core+4n nuclei respecting solely the Pauli principle.

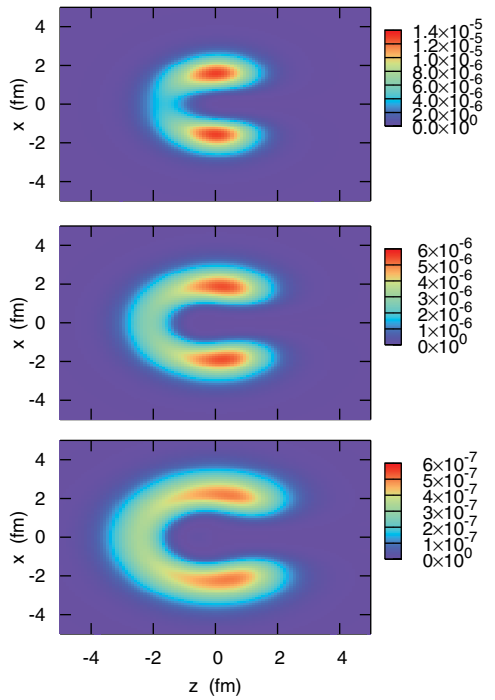

FIG. 8. (Color online) The four-particle density of ^{8}He for the dineutron-dineutron configuration when the first dineutron is on the z-axis. The top, middle, and bottom panels correspond to the cases where the first dineutron is at $z = 1.5$, 2.5, and 3.5 fm, respectively.

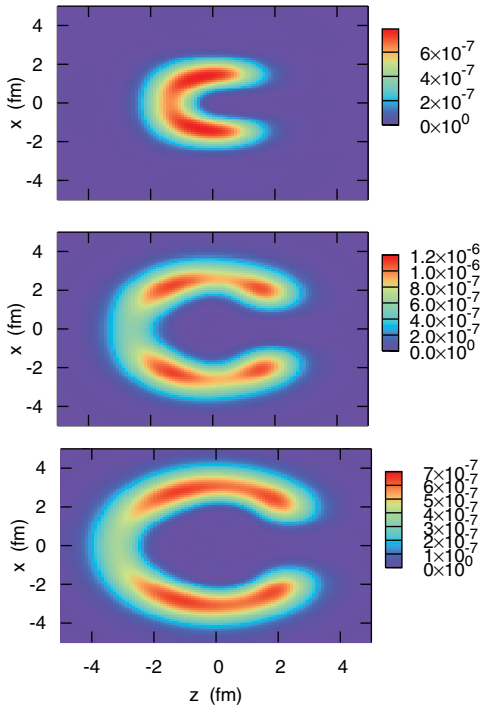

FIG. 9. (Color online) Same as Fig. 8, but for ^{18}C.

Note that the pairing interaction yet plays an essential role in the two-particle density. Without the pairing correlation, the two-particle density for the uncorrelated wave functions has symmetric bumps both around $\theta \sim 0$ and $\theta \sim \pi$, as is shown in the upper panel in Figs. 6 and 7 (see also the middle panels, that show the two-particle density with the weight of $8\pi^2 r^4 \sin\theta$). The pairing correlation mixes several angular momentum components in the ground state wave function, eliminating essentially the bump around $\theta \sim \pi$. The configuration mixing of different parity states seen in Table III is essential to have the dineutron peak in the middle panel of Figs. 4 and 5.

Another way to investigate the four-particle density is to plot the density distribution of the second dineutron when the first dineutron is put on the z-axis [9], rather than assuming that the distance from the core nucleus is the same between the two dineutrons. The top, middle, and bottom panels of Fig. 8 show the four-particle density of ^{8}He for the dineutron-dineutron configuration when the first dineutron is at $z = 1.5$, 2.5, and 3.5 fm, respectively. The pairing correlation is taken into account in the plot. The same plot for the ^{18}C nucleus is shown in Fig. 9. These figures demonstrate that the distance of the second dineutron from the core, r_2, increases as the distance of the first dineutron, r_1, increases, tending to $r_1 \sim r_2$. The angular distribution of the second dineutron, on the other hand, is almost independent of the position of the first dineutron. This behavior is consistent with the four-particle density shown in the bottom panels of Figs. 4 and 5.

V. SUMMARY

We have discussed the dineutron structure in the 2n halo nucleus ^{6}He as well as in the core+4n nuclei, ^{8}He and ^{18}C.

For this purpose, we employed the density-dependent contact interaction among the valence neutrons, and diagonalized the core+xn Hamiltonian ($x = 2$ for ^{6}He and $x = 4$ for ^{8}He and ^{18}C) with the Hartree-Fock-Bogoliubov (HFB) method. From the comparison with the exact solution of the three-body Hamiltonian for the ^{6}He nucleus, we found that the HFB method is satisfactory enough to discuss the spatial structure of the valence neutrons. For the ^{8}He and ^{18}C nuclei, we investigated both the two- and the four-particle densities. We showed that the two-particle density takes the largest value when the spin-up and the spin-down neutrons are at the same position, that is nothing but the manifestation of the strong dineutron correlation. With this result in mind, we particularly discussed the four-particle density for the dineutron-dineutron configuration. We found that two dineutrons weakly interact with each other, simply respecting the Pauli principle. The four-particle density of the HFB calculation in fact resembles to that for the uncorrelated wave functions. This result is entirely due to a short range nature of nuclear interaction. Namely, the two neutrons with the same spin have to be far apart in space due to the Pauli principle and thus their distance is likely larger than the range of the nuclear interaction. As a consequence, the interaction between the two dineutrons becomes weak, while the two neutrons in the *same* dineutron strongly interact with each other.

We have also discussed the probability for the single-particle configurations in the ground state wave function. Our HFB calculations indicate that the ^{8}He nucleus consists of the $[(1p_{3/2})^4]$ configuration by 34.9% and of the $[(1p_{3/2})^2(p_{1/2})^2]$ configuration by 23.7%, while the ^{18}C nucleus consists of the $[(1d_{5/2})^4]$ and the $[(1d_{5/2})^2(2s_{1/2})^2]$ configurations by 32.2% and 26.2%, respectively. The result for the ^{8}He nucleus is consistent with the recent experimental finding with the two-neutron transfer reaction, ^{8}He$(p, t)^6$He, that indicates an appreciable mixture of the configurations other than $[(1p_{3/2})^4]$, e.g., $[(1p_{3/2})^2(p_{1/2})^2]$, in the ground state of ^{8}He. It would be interesting to analyze the experimental data for the ^{8}He$(p, t)^6$He reaction with the wave function obtained in this paper. This will be a topic for a future publication.

ACKNOWLEDGMENTS

We thank J. Dobaczewski for useful discussions. This work was supported by the Japanese Ministry of Education, Culture, Sports, Science and Technology by Grant-in-Aid for Scientific Research under program no. 19740115.

[1] G. F. Bertsch and H. Esbensen, Ann. Phys. (NY) **209**, 327 (1991).
[2] J. Dobaczewski, W. Nazarewicz, T. R. Werner, J. F. Berger, C. R. Chinn, and J. Decharge, Phys. Rev. C **53**, 2809 (1996).
[3] M. V. Zhukov, B. V. Danilin, D. V. Fedorov, J. M. Bang, I. J. Thompson, and J. S. Vaagen, Phys. Rep. **231**, 151 (1993).
[4] T. Nakamura, A. M. Vinodkumar, T. Sugimoto, N. Aoi, H. Baba, D. Bazin, N. Fukuda, T. Gomi, H. Hasegawa, N. Imai, M. Ishihara, T. Kobayashi, Y. Kondo, T. Kubo, M. Miura, T. Motobayashi, H. Otsu, A. Saito, H. Sakurai, S. Shimoura, K. Watanabe, Y. X. Watanabe, T. Yakushiji, Y. Yanagisawa, and K. Yoneda, Phys. Rev. Lett. **96**, 252502 (2006).
[5] F. Barranco, P. F. Bortignon, R. A. Broglia, G. Colo, and E. Vigezzi, Eur. Phys. J. A **11**, 385 (2001).
[6] K. Hagino and H. Sagawa, Phys. Rev. C **72**, 044321 (2005); **75**, 021301(R) (2007).
[7] K. Hagino, H. Sagawa, J. Carbonell, and P. Schuck, Phys. Rev. Lett. **99**, 022506 (2007).
[8] C. A. Bertulani and M. S. Hussein, Phys. Rev. C **76**, 051602(R) (2007).
[9] M. Matsuo, K. Mizuyama, and Y. Serizawa, Phys. Rev. C **71**, 064326 (2005).
[10] N. Pillet, N. Sandulescu, and P. Schuck, Phys. Rev. C **76**, 024310 (2007).
[11] M. Matsuo, Phys. Rev. C **73**, 044309 (2006).
[12] J. Margueron, H. Sagawa, and K. Hagino, Phys. Rev. C **76**, 064316 (2007).
[13] I. Tanihata, D. Hirata, T. Kobayashi, S. Shimoura, K. Sugimoto, and H. Toki, Phys. Lett. **B289**, 261 (1992).
[14] Y. Suzuki and K. Ikeda, Phys. Rev. C **38**, 410 (1988); Y. Suzuki and Wang Jing Ju, *ibid.* **41**, 736 (1990).
[15] K. Varga, Y. Suzuki, and Y. Ohbayasi, Phys. Rev. C **50**, 189 (1994); K. Varga, Y. Suzuki, and R. G. Lovas, Nucl. Phys. **A571**, 447 (1994) .
[16] M. V. Zhukov, A. A. Korsheninnikov, and M. H. Smedberg, Phys. Rev. C **50**, R1 (1994).
[17] A. V. Nesterov, V. S. Vasilevsky, and O. F. Chernov, Phys. At. Nucl. **64**, 1409 (2001); arXiv:nucl-th/0006001.
[18] A. Adahchour and P. Descouvemont, Phys. Lett. **B639**, 447 (2006).
[19] Y. Kanada-En'yo, Phys. Rev. C **76**, 044323 (2007).
[20] N. Itagaki, M. Ito, K. Arai, and S. Aoyama (to be published).
[21] F. Catara, A. Insolia, E. Maglione, and A. Vitturi, Phys. Rev. C **29**, 1091 (1984).
[22] Y. Suzuki, H. Matsumura, and B. Abu-Ibrahim, Phys. Rev. C **70**, 051302(R) (2004).
[23] W. Horiuchi and Y. Suzuki, Phys. Rev. C **73**, 037304 (2006); **74**, 019901(E) (2006).
[24] K. Hagino and H. Sagawa, Phys. Rev. C **75**, 021301(R) (2007).
[25] N. Vinh Mau, Nucl. Phys. **A592**, 33 (1995).
[26] H. Esbensen, G. F. Bertsch, and K. Hencken, Phys. Rev. C **56**, 3054 (1997).
[27] M. Bender, K. Ruth, P.-G. Reinhard, and J. A. Maruhn, Eur. Phys. J. A **7**, 467 (2000).
[28] P. Ring and P. Schuck, *The Nuclear Many Body Problem* (Springer-Verlag, New York, 1980).
[29] J. Dobaczewski, H. Flocard, and J. Treiner, Nucl. Phys. **A422**, 103 (1984).
[30] A. Bulgac, nucl-th/9907088.
[31] K. Hagino and H. Sagawa, Phys. Rev. C **71**, 044302 (2005).
[32] J. Meng and P. Ring, Phys. Rev. Lett. **77**, 3963 (1996).
[33] M. V. Stoitsov, J. Dobaczewski, W. Nazarewicz, S. Pittel, and D. J. Dean, Phys. Rev. C **68**, 054312 (2003); http://www.fuw.edu.pl/ dobaczew/thodri/thodri.html.
[34] K. Hagino, P.-G. Reinhard, and G. F. Bertsch, Phys. Rev. C **65**, 064320 (2002).

[35] Yu. L. Parfenova, M. V. Zhukov, and J. S. Vaagen, Phys. Rev. C **62**, 044602 (2000).
[36] J. Dobaczewski and W. Nazarewicz, Prog. Theor. Phys. Suppl. **146**, 70 (2002).
[37] J. Dobaczewski, W. Nazarewicz, and M. V. Stoitsov, Eur. Phys. J. A **15**, 21 (2002).
[38] E. Liatard, J. F. Bruandet, F. Glasser, S. Kox, T. U. Chan, G. J. Costa, C. Heitz, Y. Elmasri, F. Hanappe, R. Bimbot, D. Guillemaudmueller, and A. C. Mueller, Europhys. Lett. **13**, 401 (1990).
[39] N. Keeley, F. Skaza, V. Lapoux, N. Alamanos, F. Auger, D. Beaumel, E. Becheva, Y. Blumenfeld, F. Delaunay, A. Drouart, A. Gillbert, L. Giot, K. W. Kemper, L. Nalpas, A. Pakou, E. C. Pollacco, R. Raabe, P. Roussel-Chomaz, K. Rusek, J.-A. Scarpaci, J.-L. Sida, S. Stepantsov, and R. Wolski, Phys. Lett. **B646**, 222 (2007).